DEVELOPMENT OF A NOVEL MATERIAL MONTMORILLONITE SUPPORTED BISMUTH VANADATE NANORODS HETEROSTRUCTURE WITH HIGHLY EFFICIENT PHOTOCATALYTIC ACTIVITY FOR THE TREATMENT OF DYE

Phyu Phyu Tun[*]

Abstract

Clay minerals supported semiconductor based photocatalysts have drawn wide attention for its economical, feasible and excellent reaction activity in photocatalytic process and for the detoxification of environmental pollutants. In this study, visible-light responsive montmorillonite (MMT) supported $BiVO_4$ heterostructure photocatalyst having superb photocatalytic activity was synthesized via typical hydrothermal method. The optimum nanocomposite with 40 wt% $BiVO_4$/MMT exhibited around 4.17 times higher photodecomposition efficiency for Methylene-blue (MB) over the as-synthesized bare $BiVO_4$, respectively. The enhancement of photocatalytic activity could be credited to sound absorption of visible light spectrum due to the narrow bandgap of $BiVO_4$, formation of additional active sites and enlarged specific surface area facilitated by MMT support, and strong interface interaction between $BiVO_4$ and MMT which is confirmed by XPS analysis. The catalyst efficiently performed well over a wide pH scale range 3-10 in the photodecomposition process. Moreover, the possible photocatalytic mechanism of $BiVO_4$/MMT nanocomposite towards the degradation progress was discussed and inferred that both $^\bullet O_2-$ and $^\bullet OH$ were dominant reactive species. The study might provide insight in designing visible-light driven clay minerals supported semiconductor based photocatalyst system for the wastewater treatment and environmental remediation.

Keywords: Photocatalytic action; Bismuth vanadate; Montmorillonite; Methylene-blue

Introduction

The prominent increase in the application of antibiotics and organic pollutants, and their direct emissions have emerged as a big threat to human health and global environment (Huang et al. 2015). Various types of technologies have been introduced for the detoxification of these environmental pollutants, in which semiconductor-based photocatalysis is one of the most lucrative, green, excellent reaction activity, low cost and highly stable technology for the decomposition of environmental contaminants. Visible light responsive photocatalysis efficiently harnesses the visible light spectrum from the abundant solar energy and convert the pollutants into harmless products. The different approaches and tactics have been developed to attain this motive, like heterojunction structure formation, morphological modification, impurity doping, coupling semiconductor, and co-catalyst loading (Long, Cai, and Kisch 2008; Wang et al. 2012; Tsuzuki et al. 2019). In recent years, although varieties of semiconductor photocatalysts have been recognized for photocatalytic removal of antibiotics and organic dyes, visible light-responsive photocatalysis having excellent activity are still in demand.

Amongst several photocatalysts, bismuth-based semiconductor materials are one of the promising photocatalyst due to their proficient exploitation of visible light, nontoxicity and high chemical stability. Recently, Bismuth Vanadate ($BiVO_4$) has attracted wide attention, is a metal oxide n-type semiconductor, reveals superb photocatalytic activity under visible light spectrum and has relatively narrow band gap for monoclinic scheelite (2.4-2.5 eV) crystalline form. The foundation of such improved visible-light photo reactivity of $BiVO_4$ led by the transformation from a valence band created by Bi 6s or a Bi 6s and O 2p hybrid orbital to a V 3d conduction band and its narrower bandgap. Additionally, as compared to similar semiconductors (e.g. In_2O_3

---

[*] Department of Industrial Chemistry, West Yangon University, Myanmar

or TiO_2), the estimated effective masses of electrons and holes of $BiVO_4$ is lower, resulting in the principle of an enriched separation and migration course of electron/hole pairs (Zhao, Li, and Zou 2011; Park, McDonald, and Choi 2013; Walshetal.2009).

Recent researches have been reported that interlinking semiconductor with apposite substrate such as carbon spheres, graphene, fly ash chemosphere's, multi-walled carbon nanotube and clay minerals owns many enhancements in photocatalytic action; improvement in the activity of semiconductor potential, formation of more active sites, aversion particle aggregation, enhancement the adsorption ability of pollutants and larger specific surface area. Montmorillonite (MMT) is the 2:1 layer structure clay mineral member of smectite clay family, formed one octahedral Al-O (Mg-O) sheet sandwiching between two tetrahedral Si-O sheets Thus, by incorporating $BiVO_4$ on MMT surface as support can attain improved visible light responsive photocatalytic activities. MMT matrix boost in the formation of more active centers with large surface area, which inhibits in the loss of catalyst through recycling and recovery process which marks more effective in practical applications (Tun et al. 2020).

This study created a $BiVO_4$/MMT nanocomposite by hydrothermally embedding nanosized $BiVO_4$ on sheets of montmorillonite matrix. As a model pollutant, methylene blue (MB) was selected, and the photocatalytic effectiveness of a synthetic photocatalyst under visible-light irradiation on the removal of MB was examined. A series of photocatalysts prepared by varying the content of $BiVO_4$ and their influence on photocatalytic activity was analyzed, and some other influencing factors were also evaluated.

Materials and Methods

Materials

The pristine Montmorillonite K-10, bismuth (III) nitrate pentahydrate (Bi $(NO_3)_3.5H_2O$), ammonium metavanadate (NH_4VO_3), nitric acid (HNO_3), urea and ammonium hydroxide ($NH_3.H_2O$) were used and obtained from Suzhou, Jiangsu Province, China for this study. All chemicals were analytical grade and used without any additional purification. Distilled water and deionized water were used as required in the experiments.

Preparation of Photocatalyst

The $BiVO_4$/MMT photocatalysts were synthesized by hydrothermal method. Approximately 2 mmol of (Bi $(NO_3)_3.5H_2O$) was dissolved in 15 ml of HNO_3 solution, and titled as A. After magnetic stirring for 30 min, a white color solution was formed. Simultaneously, 2 mmol of NH_4VO_3 was dispersed in 15 ml of HNO_3 solution and continuously stirred for 30 min and titled as B. A bright yellow turbid solution was formed after mixing solution A and B. That solution was added to 2 g of MMT solution prepared by dissolving in 50 ml of distilled water and ultrasonicated for 1 h. Then, the mixture was vigorously stirred for 1 h at room temperature. Afterwards, 0.75 g urea was mixed to the combined solution and $NH_3.H_2O$ was used to adjust the solution pH to 7. The mixture was transferred into a Teflon-lined stainless-steel vessel and subsequently heated at 200 ℃ for 6 h. After that, the resulting material was washed with distilled water and dried for 8 h in a hot air oven at 70 ℃. Next, as-prepared $BiVO_4$/MMT nanocomposite was calcined at 400 ℃ for 3 h and the final $BiVO_4$/MMT photocatalyst was obtained. In order to investigate the photocatalytic performance, ratios of $BiVO_4$/MMT nanocomposites, 10%, 20%, 40%, and 60% $BiVO_4$/MMT were synthesized via the similar process by changing the amounts of $BiVO_4$, and denoted as BVO/M-10, BVO/M-20, BVO/M-40 and BVO/M-60 respectively. For comparison dedications, the pristine material $BiVO_4$, was prepared without adding MMT.

Characterization

The X-ray diffraction (XRD) analysis (DW-XRD-Y3000) was performed to analyze the crystal plane and phase structure. The morphology and size of as-synthesized photocatalysts were examined by Scanning Electron Microscope (SEM) (JSM 5610LV). As-prepared sample morphologies and microstructures were investigated by transmission electron microscopy (TEM) (HT7800) along with an energy-dispersive X-ray (EDX) at 200kV accelerating voltage. Fourier transform infrared (FT-IR) spectroscopy (EGA4000) was used to analyze the presence of structural units and functional groups. The X-ray photoelectron spectroscopy (XPS) (ULVAC-PHI 5000, Shimadzu.Japan) study was performed using an ESCALAB II XPS system with a source of monochromatic Mg Kα and a neutralizer of charge. The Brunauer-Emmett-Teller (BET) (Horiba SA-9600) was used to measure the surface area and porosity. The catalysts absorption surface was defined by the UV-visible spectrophotometer (UV2550, 200-800 nm, Shimadzu,Japan) (DRS).

Results and Discussion

XRD Analysis

Fig. 1 illustrates the XRD pattern of the prepared samples to observe the crystal plane and phase structure. The MMT matrix displayed strong typical diffraction peak at 2θ degree ~8º could be fixed to (0 0 1) crystal plane that demonstrates the interlayered-stacking structure characteristics in MMT (Djowe et al. 2013). The observed diffraction peaks at 2θ value 18.91, 28.89, 30.57, 34.55, 35.12, 39.81, 42.44, 46.76, 50.40 and 53.39 in the pattern of $BiVO_4$ which can be indexed as (0 1 1), (1 2 1), (0 4 0), (2 0 0), (0 0 2), (2 1 1), (0 5 1), (2 4 0), (2 0 2) and (1 6 1) crystal planes, respectively, are well matched with standard monoclinic $BiVO_4$ (JCDPS file no. 14-0688). The XRD pattern of all BVO/M nanocomposite samples unveiled the diffraction peaks of $BiVO_4$. Moreover, the diffraction peak d (0 0 1) intensity of BVO/M composite get weaken and moved towards the higher 2θ value signifying that $BiVO_4$ is well overloaded on the surface of MMT structure.
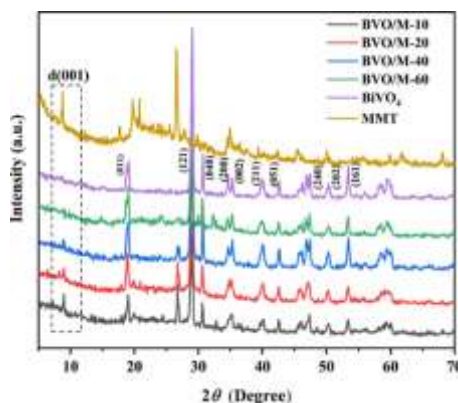
Figure.1. XRD patterns of MMT, pure $BiVO_4$ and a series of $BiVO_4$/MMT nanocomposites.

Morphological Interpretation

The surface morphological study of prepared nanocomposites was conducted by SEM and HR-TEM analysis. In MMT (Figure. 2a), layered platelet like structure comprising microscale flakes in aggregated morphology was witnessed while in pure $BiVO_4$ (Figure. 2b), leaf like with branches and trunks were observed. The $BiVO_4$ nanoparticles with average particle size 129 nm are dispersed over the surface and interspace of MMT. Upon incorporation of $BiVO_4$ on MMT surface, the trunks and branches of the $BiVO_4$ disappeared showing nanorod like

structure and partially crackdown layered structure of MMT were observed in the BVO/M-40 nanocomposite (Figure. 2c, d). Moreover, the HR-TEM images Figure. 2e, f reflect the lattice phase and crystallographic plane of BVO/M-40 nano-composite. The identified lattice spacing of 0.212 nm and 0.467 nm corresponds to the (0 5 1) and (0 1 1) crystallographic plane of BiVO$_4$ respectively, which is in good agreement with the XRD analysis. The energy dispersive X-ray analysis (Figure. 3) validates that as synthesized BVO/M-40 nanocomposite consists of Bi, O, V, Si, Al, Mg and Fe as dominant species which shows the sound evidence of the successful synthetization of BiVO$_4$/MMT nanocomposite.
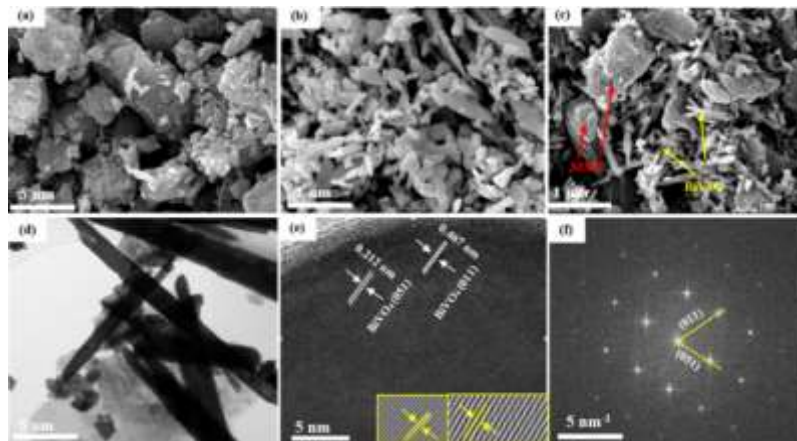
Figure.2. SEM images of (a) MMT, (b) BiVO$_4$, (c) BiVO$_4$/MMT, and (d) TEM images, (e) HRTEM image of BiVO$_4$/MMT, the insets are HRTEM image of lattices of BiVO$_4$, and (f) Selective area electron diffraction (SAED) showing well resolved lattice fringes of BiVO$_4$.
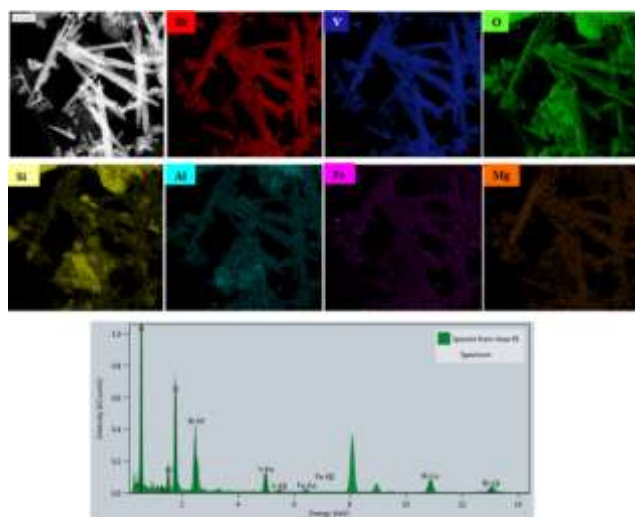
Figure.3. The HRTEM image of BiVO$_4$/MMT and the corresponding EDX mapping images

BET Analysis

N$_2$ adsorption examination was performed to determine the porosity and specific surface area of as-synthesized photocatalysts (Fig.4). The BJH curves appear to be type IV isotherms and display a H3 hysteresis loop, which indicates mesoporosity in the photocatalyst (2-50 nm) (Manova et al. 2010). The pore size distribution graph further ratified the mesoporous size distribution in the materials (inset in the Fig. 4) and have majority of the available pores smaller

than 10 nm. The BET surface area and pore volume of MMT were calculated to be about 248.01 m^2/g and 0.397 cm^3/g and the composite BVO/M-40 were approximately 247.02 m^2/g and 0.416 cm^3/g, respectively (Table 1). Upon overloading $BiVO_4$, the specific surface area of BVO/M-40 nanocomposite was maintained at high level with no drastic fall down. The BET surface area of BVO/M-40 nanocomposite is higher than $BiVO_4$ NPs (80.2 m^2/g) that suggests interlaminar configuration and sound adsorption ability of MMT which constructed extra active centers and enlarged specific surface area.
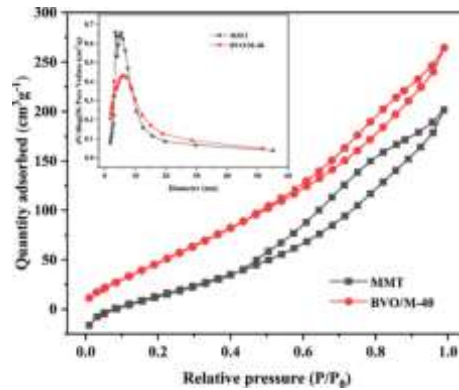
Figure 4. N_2 adsorption-desorption isotherms and the pore size distribution plot of montmorillonite and $BiVO_4$/MMT-40 nanocomposite.

Table 1 BET specific surface area and pore size data of the MMT and BVO/M-40 nanocomposite.

Sample	S_{BET} (m^2/g)	Pore Volume (cm^3/g)	Pore Size (nm)
Pure MMT	248.01	0.397	6.4
BVO-M/40 nanocomposite	247.02	0.416	6.7

UV- Visible DRS

        Figure. 5a shows how the photo-absorption abilities of as-synthesized photocatalysts were investigated using UV-visible spectroscopy. The MMT matrix displayed 250-350 nm broadband absorption characteristics. These bands might be allocated to charge transferal band for the existing ions in the clay mineral octahedral layer (Rao and Mishra 2002).
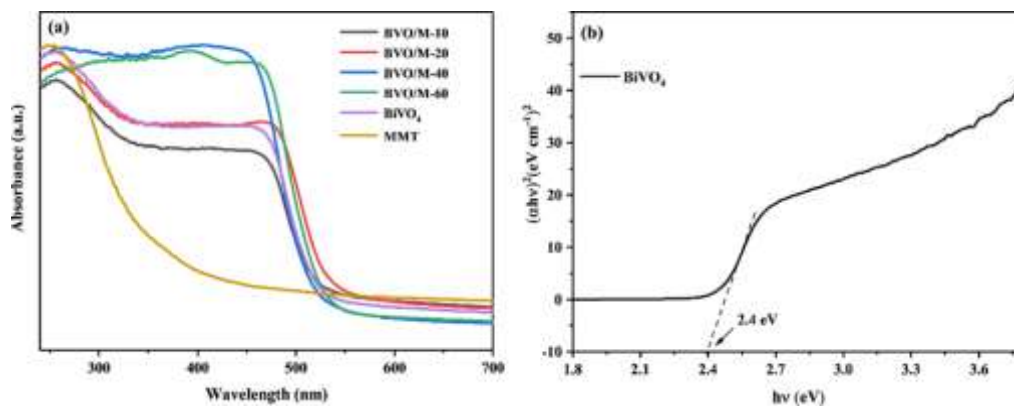
Figure.5. (a) UV-vis Diffuse reflectance spectra of MMT, $BiVO_4$, and a series of $BiVO_4$/MMT composites and (b) Plot of $(\alpha h\nu)^2$ versus photon energy $h\nu$ for $BiVO_4$.

        The configuration of Si-O tetrahedron silicate layers in the clay are not capable of absorbing light in the range of 200–700 nm except when the transition-metal ions or the silicate

structure exists in the exchanging interlayers. The pure $BiVO_4$ show absorption band edge ~530 nm and displayed fair visible-light absorption. All the $BiVO_4$/MMT photocatalysts exhibited the strong photonic absorbance in 350-550 nm region, signifying visible-light absorbance is because of the intrinsic band gap transition. The band gap (E_g) of $BiVO_4$ were measured by the Tauc-plot equation;

$$(\alpha h\nu)^2 = A(h\nu - E_g)^n$$

Where $h\nu$ is the energy of the strike photon (eV), α is the absorbance coefficient, E_g band gap (eV) and whereas A stands for a constant respectively. Here, the value of n is taken as 1 for direct transition of $BiVO_4$. The estimated band gap of $BiVO_4$ was 2.4 eV (Fig.5b). This analysis reflected that BVO/M-40 nanocomposite could proficiently exploit the visible light.

XPS –Analysis

The high-resolution XPS spectra analysis was conducted to inspect the oxidation state and surface composition of BVO/M nanocomposites. Fig. 6a shows the XPS survey spectra of BVO/M-40, which validated the existence of O, V, Bi, Al, Si and C, as key elements in the nanocomposite. In the spectrum of $BiVO_4$, Bi 4f display two peaks at binding energies 164.4 and 159.1 eV corresponding to the peaks of Bi $4f_{7/2}$ and Bi $4f_{5/2}$ in as Bi^{3+} state respectively. While BVO/M nanocomposite exhibited the peaks of Bi $4f_{7/2}$ and Bi $4f_{5/2}$ at binding energies 164.2 and 158.99 eV (Fig. 6b). The slight backward shift in binding energy of 0.2 eV along with decreased intensities in BVO/M nanocomposite reflects strong interaction. In the XPS spectra of Bi 4f, no other peaks were further detected, that inferred bismuth occurred in only +3 oxidation state. The XPS peaks of $BiVO_4$ could be fitted into two peaks of V $2p_{3/2}$ and V $2p_{1/2}$ at binding energies 516.63 and 524.17 eV respectively (Fig.6c), and can be ascribed to the surface V^{5+} species . In fig. 6d, the XPS of O 1s of the $BiVO_4$ fitted into two peaks at binding energies at 531.74 and 530.66 eV which could be correspond to the Bi-O and V-O bond in the sample respectively. The O 1s spectra of BVO/M-40 display three peaks at 532.20 and 531.60 and 529.80 eV, these peaks might be ascribed to the Bi-O bond, V-O bond and Metal-O bond on the surface of MMT in the BVO/M nanocomposite, respectively. In BVO/M composite, an additional form of oxygen was found and also the peaks slightly shifted and increased the binding energies as that of $BiVO_4$ which shows the strong interaction between $BiVO_4$ and MMT structure.
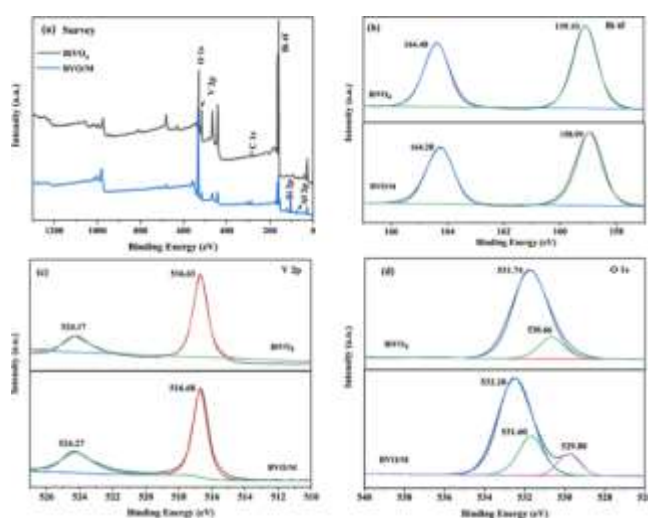
Figure.6. XPS spectra of $BiVO_4$ and $BiVO_4$/MMT-40 nanocomposite: (a) survey spectra, (b) Bi 4f spectra, (c) V 2p spectra, and (d) O 1s spectra.

FT-IR and Raman Analysis

The FT-IR spectra of as-synthesized BVO/M-40 and MMT are presented in Fig. 7a to analyze the presence of structural units and functional groups. Both samples display the distinctive absorption points of MMT in the FT-IR spectra. The spectrum of BVO/M-40 exhibits peaks at 3435, 1632, 1062, 740, 525 and 470 cm^{-1}, which are indexed to the characteristics of MMT. The bands at 3622 and 3437 cm^{-1} of MMT could be related to the characteristic stretching vibrations of –OH and adsorbed H_2O on the surface of clay, respectively. The band at 1637 cm^{-1} denotes the bending vibration and stretching of adsorbed water molecule. The tough robust absorption band at 1051 cm^{-1} is credited to Si–O stretching vibration. The absorption peaks of nanocomposite at 749 cm^{-1} and 810 cm^{-1} can be allotted to asymmetric and symmetric stretching/bending vibration of V–O (García-Pérez, Sepúlveda-Guzmán, and Martínez-de la Cruz 2012). The adsorption band at 525 cm^{-1} might display stretching vibration of Bi–O.

Additionally, Raman spectroscopy analysis was also conducted to further probe the structural vibration and bonding in metal-oxide group. Fig. 7b depicts the Raman spectra of MMT, pure $BiVO_4$ and BVO/M-40 nanocomposite. The Raman spectra of $BiVO_4$ exhibits six distinctive observable vibrational band peaks at 216, 331, 371, 644, 710 and 834 cm^{-1} that are correlated to vibrational characteristics of the VO_4 tetrahedron (Sandhya Kumari et al. 2013). The strong Raman band at 834 cm^{-1} was ascribed to the shorter symmetric V–O stretching band and weak peaks at 710 and 644 cm^{-1} could be attributed to the long and short asymmetric V–O stretching bands respectively. The symmetric and asymmetric bending bands of VO_4 tetrahedron appeared at 371 and 331 cm^{-1} respectively (Sandhya Kumari et al. 2013), and while peak at 216 cm^{-1} detected by external modes. The V–O stretching vibration band has moved to lower frequency at 828 cm^{-1} and considerably declined in BVO/M-40 nanocomposite with respect to pure $BiVO_4$ toughest peak at 834 cm^{-1}. This reflects strong synergetic interaction between MMT and tetrahedron VO_4 structure of $BiVO_4$.
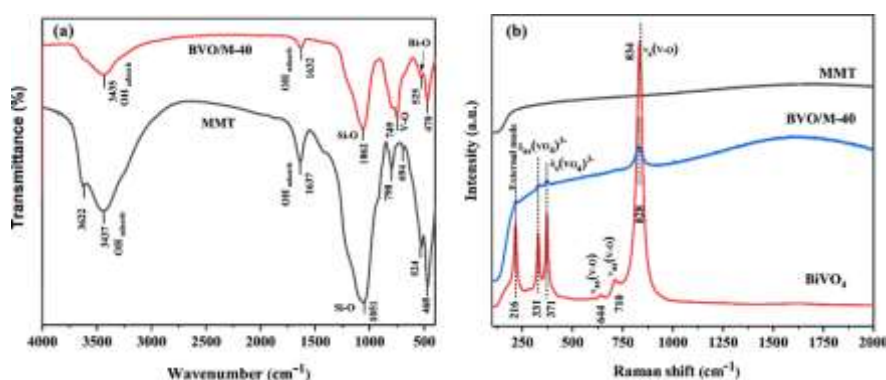
Figure.7. (a) FT-IR spectra of pristine MMT and $BiVO_4$/MMT-40 nanocomposite and (b) Raman spectra of pure BiVO4 and BiVO4/MMT-40 nanocomposite.

Photocatalytic performance for the degradation of MB and influencing factors

The photocatalytic efficiencies of as-prepared catalysts were further investigated through degrading MB (10 mg/L) under visible-light illumination (Fig. 8a). The photo-degradation of MB was virtually completely disregarded during blank test and the BVO/M-40 nanocomposite revealed fair adsorption capacity in the dark state. The photocatalytic efficiency of BVO/M-40 nanocomposite was highest among all other catalyst samples, where complete degradation of MB occurs in 30 min. Furthermore, the photocatalytic degradation of MB unveiled pseudo first order

reaction kinetics (ln (C_t/C_0) = kt). As depicted in Fig.8b BVO/M-40 nanocomposite displays utmost photodecomposition and has highest apparent rate constant k towards MB and pursue the order: BVO/M-40 (0.096 min^{-1}) > BVO/M-60 (0.044 min^{-1}) > BVO/M-20 (0.033 min^{-1}) > BVO/M-10 (0.028 min^{-1}) > BiVO$_4$ (0.023 min^{-1}) > MMT (0.008 min^{-1}).

The influence of pH was inspected on photodegradation efficiency of MB by BVO/M-40 nanocomposite photocatalyst with adjusting pH scale range 3-10. As displayed in graph Fig. 9a, the photo discoloration efficiency on MB steadily decrease from 100% to 75% while adjusting elevation of pH scale 3 to 10. The optimum discoloration efficiency was at pH 3 and all the experiments were performed at pH 3 for MB. The reaction activity of as prepared BVO/M-40 photocatalyst is suitable for wide pH range.

Additionally, the photocatalytic activity of BVO/M-40 was further assessed by considering different initial concentration of MB. As demonstrated in Fig. 9b, the photodegradation proficiency consecutively drop on increasing its concentration from 10 mg/L to 50 mg/L. However, the discoloration efficiencies of MB were still above 65%. The reduction might be due to hindrance in light absorption by the catalyst caused by excess MB molecules which restraint in the formation of oxidative agent. The impression of catalyst dosages in photocatalytic decomposition of MB were also evaluated (Fig. 9c). The minimal fall down in photo discoloration efficiency was observed while increasing the concentration of catalyst 0.5 g/L to 1.0 g/L. It might be due to reaction turbidity in the system.
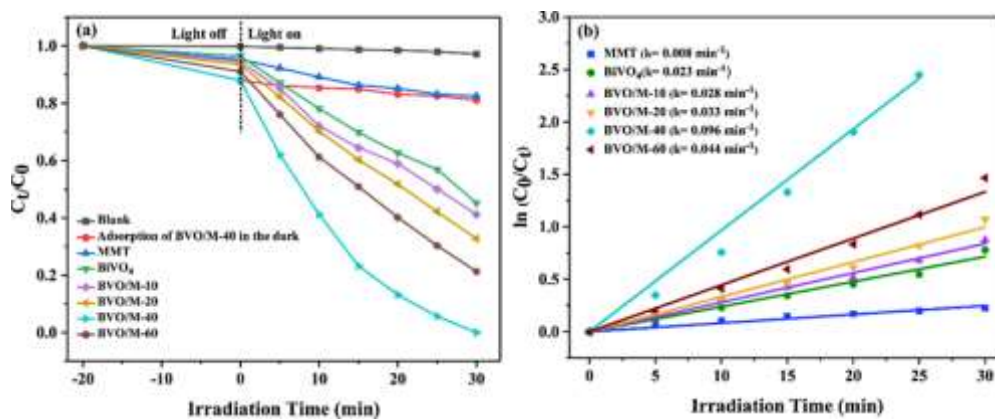
Figure.8. (a) Degradation efficiency of MB (20 mg/L), and (b) the relationship between ln (C_0/C_t) and irradiation time with pseudo first order reaction rate constant.
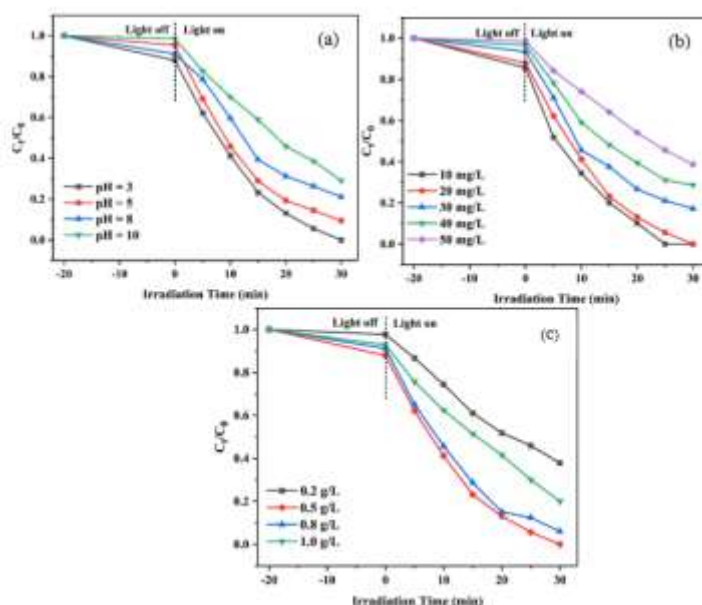
Figure.9. (a) Effect of pH, and (b) Effect of initial MB concentration, and (c) Effect of catalyst dosage on the degradation of MB in photocatalytic process.

Photocatalytic Mechanism

The mechanism for the extremely improved photocatalytic scheme can be put forward in Fig. 10 on the grounds of the above-mentioned experimental study. As BVO/M-40 nanocomposite was irradiated under visible light, $BiVO_4$ NPs get photo-excited producing e^-/h^+ pairs by forming holes in valence band (VB) and electrons in conduction band (CB). The excited electrons may reduce the O_2 molecules adsorbed on the surface of BVO/M into anionic superoxide radical $(^\bullet O_2^-)$ that can oxidize the contaminants as well as parts of $^\bullet O_2^-$ can combine with H^+ to generate H_2O_2 which further undergoes to reductive decomposition in the reaction system to produce hydroxide radicals $(^\bullet OH)$. As formed $^\bullet OH$ and $^\bullet O_2^-$ radicals are strong oxidizing agents to decompose MB directly. In addition, some amount of photoinduced holes in the VB of $BiVO_4$ oxidizes the H_2O/OH^- in the reaction system by interfacial charge transfer to form hydroxide radicals $(^\bullet OH)$ radicals. On the other side, the photo-excited electrons in the CB of $BiVO_4$ can also be trapped by Al atoms present in the montmorillonite structure. In fact, MMT matrix performs like electron acceptors because of the existence of Lewis acid (Al atoms). The trapped electrons from these aluminum sites then moved to the adsorbed O_2 molecules in the solutions. As a consequence, the recombination reaction of photogenerated e^-/h^+ pairs by hopping mechanism of electrons are delayed. Moreover, MMT enables many active centers for the adsorption of organic molecules, averts the aggregation of photocatalyst and its support reduces the high turbidity of the solution. It also provides easiness during recovery and separation process of photocatalyst.
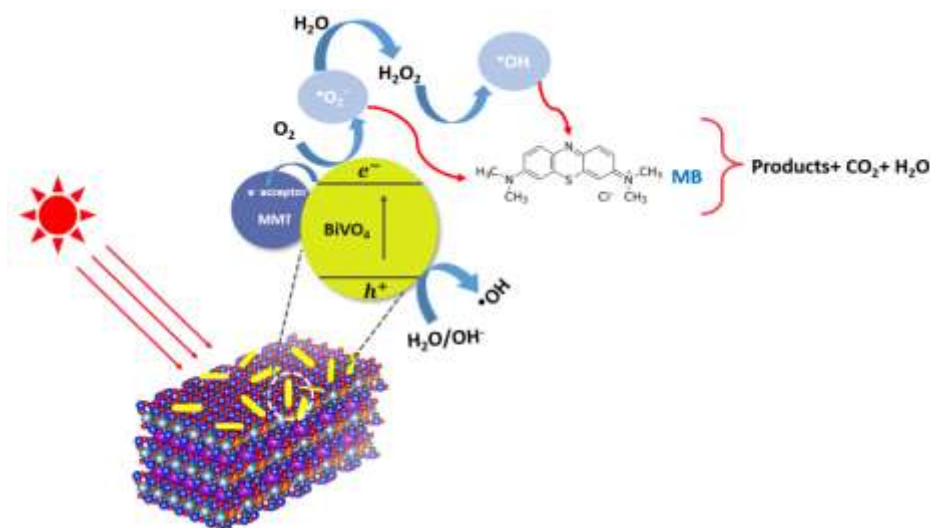
Figure.10. Schametic depiction of proposed mechanism for eletron-hole separation of BiVO₄/MMT composite under visible light irradiation.

Conclusion

A series of BiVO₄/MMT nanocomposites were developed by a one-step hydrothermal process, a competitive synthesis of novel and active photocatalysts were employed to decompose the dye MB as a model of evolving contaminant. The results confirmed that optimized BVO/M-40 nanocomposite exhibited superior photocatalytic activity than that of BiVO₄, MMT and BVO/M photocatalyst, which were clarified by the characterization of the as-prepared specimens through conducting XRD, HRTEM, XPS, BET, FT-IR, and UV-Vis DRS analysis. The efficient visible-light harvesting and interface interaction between the BiVO₄ and MMT synergism to enhance the photocatalytic performance that were revealed by UV-Vis DRS and XPS analysis. BET exploration suggested MMT support facilitates in the creations of more active centres and enlarged surface area for photocatalytic action. The catalyst unveiled a high-quality photocatalytic action over a broad pH 3-10 range. This is the promising properties for the as-synthesized photocatalyst for the decontamination of the wastewater toxins and also insights to design effective photocatalysts for the environmental remediation.

Acknowledgements

References

Djowe, Antoine Tiya, Samuel Laminsi, Daniel Njopwouo, Elie Acayanka, and Eric M. Gaigneaux. 2013. 'Surface Modification of Smectite Clay Induced by Non-thermal Gliding Arc Plasma at Atmospheric Pressure', Plasma Chemistry and Plasma Processing, 33: 707-23.

García-Pérez, U. M., S. Sepúlveda-Guzmán, and A. Martínez-de la Cruz. 2012. 'Nanostructured BiVO4 photocatalysts synthesized via a polymer-assisted coprecipitation method and their photocatalytic properties under visible-light irradiation', Solid State Sciences, 14: 293-98.

Huang, Manhong, Fangfang Qi, Jue Wang, Qi Xu, and Li Lin. 2015. 'Changes of bacterial diversity and tetracycline resistance in sludge from AAO systems upon exposure to tetracycline pressure', Journal of Hazardous materials, 298: 303-09.

Liu, Yuxi, Hongxing Dai, Jiguang Deng, Lei Zhang, and Chak Tong Au. 2012. 'Three-dimensional ordered macroporous bismuth vanadates: PMMA-templating fabrication and excellent visible light-driven photocatalytic performance for phenol degradation', Nanoscale, 4: 2317-25.

Long, Cai, and Horst Kisch. 2008. 'Visible Light Induced Photoelectrochemical Properties of n-BiVO4 and n-BiVO4/p-Co3O4', The Journal of Physical Chemistry C, 112: 548-54.

Manova, Elina, Pilar Aranda, M. Angeles Martín-Luengo, Sadok Letaïef, and Eduardo Ruiz-Hitzky. 2010. 'New titania-clay nanostructured porous materials', Microporous and Mesoporous Materials, 131: 252-60.

Park, Y., K. J. McDonald, and K. S. Choi. 2013. 'Progress in bismuth vanadate photoanodes for use in solar water oxidation', Chemical Society Reviews, 42: 2321-37.

Rao, G. Ranga, and Braja Gopal Mishra. 2002. 'Mixed Al/Ce oxide pillaring of montmorillonite: XRD and UV-VIS diffuse reflectance study', Reaction Kinetics and Catalysis Letters, 75: 251-58.

Sandhya Kumari, L., P. Prabhakar Rao, A. Narayana Pillai Radhakrishnan, Vineetha James, S. Sameera, and Peter Koshy. 2013. 'Brilliant yellow color and enhanced NIR reflectance of monoclinic BiVO4 through distortion in VO4− tetrahedra', Solar Energy Materials and Solar Cells, 112: 134-43.

Tsuzuki, Takuya, Rongliang He, Aaron Dodd, and Martin Saunders. 2019. 'Challenges in Determining the Location of Dopants, to Study the Influence of Metal Doping on the Photocatalytic Activities of ZnO Nanopowders', Nanomaterials, 9.

Tun, Phyu Phyu, Junting Wang, Thinn Thinn Khaing, Xiaoyong Wu, Gaoke Zhang, Journal of Alloys and Compounds. 2020. 'Fabrication of functionalized plasmonic Ag loaded Bi2O3/montmorillonite nanocomposites for efficient photocatalytic removal of antibiotics and organic dyes', 818: 152836.

Walsh, Aron, Yanfa Yan, Muhammad N. Huda, Mowafak M. Al-Jassim, and Su-Huai Wei. 2009. 'ChemInform Abstract: Band Edge Electronic Structure of BiVO4: Elucidating the Role of the Bi s and V d Orbitals', ChemInform, 40.

Wang, Donge, Rengui Li, Jian Zhu, Jingying Shi, Jingfeng Han, Xu Zong, and Can Li. 2012. 'Photocatalytic Water Oxidation on BiVO4 with the Electrocatalyst as an Oxidation Cocatalyst: Essential Relations between Electrocatalyst and Photocatalyst', The Journal of Physical Chemistry C, 116: 5082-89.

Zhao, Z., Z. Li, and Z. Zou. 2011. 'Electronic structure and optical properties of monoclinic clinobisvanite BiVO4', Physical Chemistry Chemical Physics, 13: 4746-53.